Volume 1 | Number 1 | Jan 2013 | Pages 1–100

Metallomics

Integrated biometal science
www.rsc.org/metallomics

ROYAL SOCIETY OF CHEMISTRY

ROYAL SOCIETY OF CHEMISTRY

www.rsc.org/metallomics

Metallomics

ARTICLE

Roles of *Escherichia coli* ZinT in cobalt, mercury and cadmium resistance and structural insights into the metal binding mechanism

H. G. Colaço,[a] P. E. Santo[b], P. M. Matias,[b,c] T. M. Bandeiras[b,c] and J. B. Vicente[c]

Escherichia coli ZinT is a metal binding protein involved in zinc homeostasis, with additional putative functions in the resistance against other metals. Herein, a method was designed and implemented to evaluate from a structural and functional viewpoint metal binding to *E. coli* ZinT in 96-well microtiter plates. The isolated ZinT was mixed with several metal ions and their binding ability was determined by differential scanning fluorimetry. From the positive hits, six metal ions were evaluated in terms of their toxicity towards an *E. coli* strain depleted of ZinT (Δ*zinT*) using as control a strain deleted in the *galT* gene (Δ*galT*). The different sensitivities of each strain to the tested metals revealed novel roles of ZinT in the resistance to cobalt, cadmium and mercury. This approach provides a valuable and reliable platform for the analysis of metal binding and its functional implications, extendable to other metal binding proteins. In combination with the developed platform, structural studies were performed with ZinT, with the zinc-loaded crystallographic structure being obtained at 1.79 Å resolution. Besides the canonical zinc-binding site located near the N-terminus, the herein reported dimeric ZinT structure unravelled extra zinc binding sites that support its role in metal loading and/or transport. Altogether, the designed experimental platform allowed revealing new roles for the ZinT protein in microbial resistance to heavy metal toxicity, as well as structural insights into the ZinT metal binding mechanism.

Introduction

Metals are essential for the survival of all forms of life, participating in numerous metabolic processes that rely on metalloproteins. However, high concentrations of metals are responsible for severe cellular damage. In bacteria, the importance of metal toxicity is illustrated by the use of mercury, silver or copper as antibacterial agents for centuries and the recent development of new metal-based strategies for controlling infections [1, 2]. Mechanisms of metal toxicity towards bacterial cells often include the displacement of other metals from their active sites. Among the most common targets for ligand exchange are zinc finger proteins, essential for transcription, DNA repair or protein folding, which are particularly prone to electrophilic attack by excess cadmium and cobalt, often resulting in loss of function [3]. Iron-sulfur clusters are also targets for metals with high reactivity towards sulfhydryl moieties [4, 5]. Depending on their ability to react with sulfur (greater for mercury, silver, copper, cadmium and zinc), metals may displace iron from fully-assembled Fe-S clusters, impairing enzymatic activity [5]. Furthermore, even less thiophyllic metals such as cobalt are able to compete with iron for the Fe-S assembly during the *de novo* synthesis of these clusters [6]. A number of direct and indirect toxicity mechanisms of metals towards bacteria have also been described. Copper, iron and, to a lesser extent, cobalt are able to undergo Fenton-like reactions, which generate reactive oxygen species (ROS), therefore increasing oxidative stress [4, 6]. The produced free radicals attack nucleic acids, proteins and membranes and might even react with protein Fe-S clusters, thus feeding the cascade of toxic events [7]. Additionally, there is evidence for reactions of nickel and cadmium with DNA and proteins involved in nucleic acid synthesis and repair, pointing to further direct cytotoxic effects [8, 9].

The fine balance required to maintain intracellular levels of all metals that meet metabolic needs without exerting toxic effects led to the development of several regulatory mechanisms in bacteria. These include a complex network of transport systems as well as metal-sensing transcriptional regulators (reviewed in [10-12]). A transcriptional analysis of *E. coli* cultured in the presence of cadmium [13] has allowed the identification of a cadmium-induced product of the ORF0216, named YodA [14] and later renamed ZinT.

ZinT is a 216-amino acid protein found in the cytoplasm of bacteria, which undergoes translocation to the periplasm upon cadmium stress. This process is thought to involve the cleavage of an N-terminal signal peptide, yielding a 22.3-KDa mature protein [14, 15]. The ZinT sequence is conserved among several bacterial species (Supplementary Figure S1) and the crystal structures obtained for *E. coli* [16] and *Salmonella* (*S.*) *enterica* [17], the only available, revealed extraordinary structural similarities.

Functional studies using *E. coli zinT*-deleted mutant strains showed that ZinT has an important role in dealing with zinc-deficient conditions [18, 19]. Similar studies where cells were grown at high concentrations of metals showed contradictory conclusions regarding a putative role of ZinT in cadmium and copper resistance [20, 21]. Expression of *zinT* is dependent on both the oxidative stress regulator SoxS and the metalloregulators Fur and Zur [14, 22]. The Zur-regulated expression of ZinT affords a defence mechanism in response to zinc shortage, which also involves the ZnuABC complex [23]. At low intracellular zinc concentrations, the zinc-depleted Zur de-represses *zinT* and *znu* [22, 23], increasing ZinT and ZnuABC expression, thus leading to increased zinc import. Despite the role of ZinT in this process remaining unclear, recent studies proved a close relationship between ZinT and ZnuA, where ZinT uses its high affinity for zinc [19] to accumulate ions and transfer them to the zinc import complex [18, 24, 25]. Regulation of ZinT expression is not limited to zinc availability, as seen by the increased protein accumulation in response to cadmium stress. This up-regulation is primarily dependent on SoxS, indicating an indirect effect of cadmium-mediated ROS [14], but might also result from cross-reactivity of divalent metals with Fur and Zur [18, 20, 26].

Despite the existing information about ZinT function, its physiological role in metal metabolism is still not completely clear. ZinT and ZnuA seem to have a redundant function in zinc recruitment from the periplasm, with many bacteria lacking ZinT and relying only on ZnuABC for zinc import [25]. Moreover, the initial observation that ZinT expression is up-regulated by cadmium and the fact that the protein has high affinity for several divalent metals point to a role in metal detoxification, which has not been demonstrated.

Herein we used two 'high'-throughput methods employing 96-well plates to assess metal binding to ZinT and evaluate their functional effect in a *zinT*-deleted *E. coli* strain. Differential scanning fluorimetry (DSF) allowed us to screen a library of metals for their ability to bind purified ZinT and select positive hits. Next, by growing cells in 96-well plates, we were able to evaluate the toxicity of a wide range of metal concentrations. These straightforward procedures, which may easily be employed in the future with other metalloproteins, allowed us to identify a new role for ZinT in cobalt, mercury and cadmium resistance, opening new perspectives for the function of this versatile protein. A complementary structural analysis revealed the presence of extra metal binding sites besides the canonical clusters previously identified in ZinT, which are herein discussed in light of the possible role of ZinT as an efflux system.

Results and Discussion

Serendipitous isolation of ZinT due to a 'natural' His-tag

Purified ZinT was unexpectedly obtained while attempting to express a protein of unknown function from the protozoan pathogen *Entamoeba histolytica* (879.m, encoded by the gene EHI_16450), using *E. coli* as heterologous expression system. Interestingly, the accidental isolation of this protein has been previously reported [15, 27] and likely results from the presence of a partially conserved natural N-terminal sequence HGHHSH in ZinT (red box in Supplementary Figure S1) that mimics the hexa-histidine tag commonly used for protein purification by affinity chromatography in nickel resins. This peptide sequence actually becomes the N-terminus of the mature ZinT. In fact, ZinT (formerly known as YodA) was classified among the proteins requiring higher imidazole concentrations to be eluted in metal ion affinity chromatography columns, making it one of

the most common contaminants in this type of protein purification step [27]. Intracellular accumulation of ZinT in *E. coli* is increased under zinc starvation conditions [18], which is the case of the chemically defined medium M9 (without zinc supplementation) herein used to culture the bacteria. Therefore, it is likely that levels of ZinT surpass those of the 879.m protein, probably due to lower expression level and/or lower solubility of the latter, thus explaining ZinT as the single 22-KDa product obtained after purification. ZinT was isolated as a homodimer, as judged by size-exclusion chromatography.

ZinT binds an array of divalent metals

Screening of metals binding to ZinT was performed by differential scanning fluorimetry (DSF) using the probe SYPRO Orange, which binds to the protein's hydrophobic residues and fluoresces upon thermal denaturation of the protein. The inflexion point from a sigmoidal thermal denaturation curve defines the protein's melting temperature, T_m under a given condition.
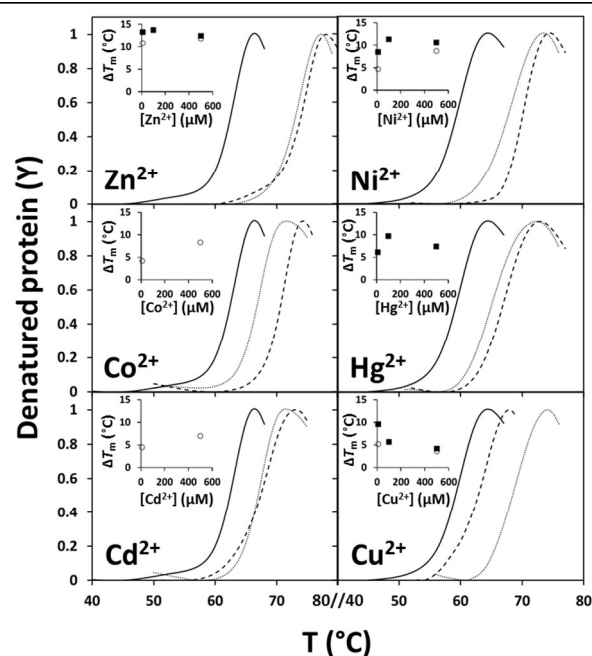

Figure 1. Heavy metals have an impact on *Escherichia coli* ZinT thermal stability. Binding of heavy metals to *E. coli* ZinT was assessed by DSF thermal denaturation assays. Normalized denaturation curves obtained from a linear temperature gradient of 0.1°C/sec (Zn^{2+}, Co^{2+} and Cd^{2+}) or 1°C/min (Ni^{2+}, Hg^{2+} and Cu^{2+}) in a reaction mixture containing 0.2 μg/μL purified ZinT in HEPES 100 mM pH 7.0, SYPRO orange (1:1000) and different metal concentrations: 0 μM (full lines), 10 μM (dotted lines) and 500 μM (dashed lines). Each curve results from the average of three denaturation curves. Insets show the shift in T_m as a function of metal concentration, obtained with the 0.1°C/sec (hollow circles) and 1°C/min (full squares) gradients.

The assumption that ligand binding alters the protein's conformational stability, either increasing or decreasing the T_m, allowed us to identify binding of metals to ZinT when the |ΔT_m| ± S.D. ≥ 2 °C. From the tested metals (10-500 μM, Supplementary Table 1), a restricted group of divalent metals was found to result in an increased thermal stability of ZinT, indicative of those metals specifically binding to the protein (Figure 1). The final buffer composition in the protein mixture affords a salt concentration altogether ~300-15,000-fold excess

over the metal counter-ions at the tested concentrations, confirming that the observed thermal shifts result from metal binding to ZinT. Notably, a high shift in T_m was observed at the lowest metal concentration tested (10 μM), approximately equimolar with ZinT (9 μM), which indicates high affinity for the metals.

Zinc showed the highest increase in ZinT thermal stability (+10.8 ± 0.3°C at 10 μM Zn^{2+}) (Figure 1; Supplementary Table 1), no further increase being observed at a higher concentration (500 μM). The maximal effect obtained at a low concentration of metal is in accordance with previous studies pointing out the high affinity binding of zinc to ZinT using size-exclusion chromatography [19], mass spectrometry [20] and fluorimetry [17]. Nickel binding to ZinT also resulted in a significant increase in T_m even at the lowest concentration (10 μM Ni^{2+}; +8.5 ± 0.3°C) and a higher effect at 500 μM (+10.6 ± 0.1°C) (Figure 1; Supplementary Table 1). High affinity for nickel has been described when ZinT was first crystallized, as nickel ions from the resin used for affinity purification were found in the protein 3D structure even when the metal was absent from the crystallization conditions [16]. Regarding cadmium binding, we observed a concentration-dependent increase in T_m of 4.5 ± 0.2°C at 10 μM Cd^{2+} up to 7.0 ± 0.3°C at 500 μM (Figure 1; Supplementary Table 1). The first studies with purified ZinT [16] followed by cellular assays using radiolabelled cadmium revealed high affinity for Cd^{2+}, leading researchers to believe that the main role of ZinT would be related to cadmium stress resistance [21]. However, a more recent experiment comparing the elution profile of Cd- and Zn-bound ZinT by size-exclusion chromatography showed that the protein favors binding of zinc over cadmium [19]. Similarly to cadmium, cobalt increased the T_m by 4.2 ± 0.0°C at 10 μM and 8.3 ± 0.1°C at 500 μM (Figure 1; Supplementary Table 1). In a previous study, Kershaw and co-workers observed no binding of Co^{2+} to ZinT at 0.1 molar equivalents of metal [20]. By increasing the metal concentration to 10 μM (~1 molar equivalent) or higher, we were able to observe a significant shift in thermal stability. Contrarily, binding of mercury occurred even at the lowest concentration tested, causing an upshift in the T_m of 6.1 ± 0.3°C at 10 μM and a slight increase at 500 μM (+7.4 ± 0.1°C) (Figure 1; Supplementary Table 1). Again, these results are in accordance with those obtained by Kershaw [20] indicating binding of Hg^{2+} to ZinT at low metal concentrations. Copper also caused a significant change in thermal stability at a low concentration (+9.6 ± 0.4°C at 10 μM). However, at higher concentrations the stabilizing effect of Cu^{2+} seems to decrease, producing a ΔT_m of +4.2 ± 0.5°C at 500 μM (Figure 1; Supplementary Table 1). This effect is likely an artifact caused by optical interference of high concentrations of copper with the fluorescent probe, as observed in a control assay containing 500 μM Cu^{2+} and no protein, which resulted in an aberrant curve (data not shown). Apart from minor changes in thermal stability in the presence of manganese and strontium, no other metals were found to bind to ZinT (Supplementary Table 1). Therefore, the restricted group of metals composed by zinc, nickel, cadmium, cobalt, mercury and copper was selected for further cellular assays.

New function in cobalt, mercury and cadmium resistance

The results obtained for the metal binding to ZinT prompted us to assess the effect of these metals (at varying concentrations; Supplementary Table 2) at a cellular level using an *E. coli* ΔzinT strain. The ΔgalT mutant was chosen as a control, as it carries the same kanamycin resistance cassette as the ΔzinT strain and the *galT* gene, encoding galactose 1-phosphate

uridylyltransferase, an enzyme involved in galactose metabolism has no relation with metal trafficking and metabolism in *E. coli*.

Growth curves obtained after the addition of cobalt to early-exponential cultures show that the ΔzinT strain growth is markedly delayed at 250 μM Co^{2+} as compared to the control (Figures 2A, B and C). At 500 μM Co^{2+}, the growth of both strains is inhibited, although to a much higher extent for the ZinT-depleted strain (Figures 2A, B and D).
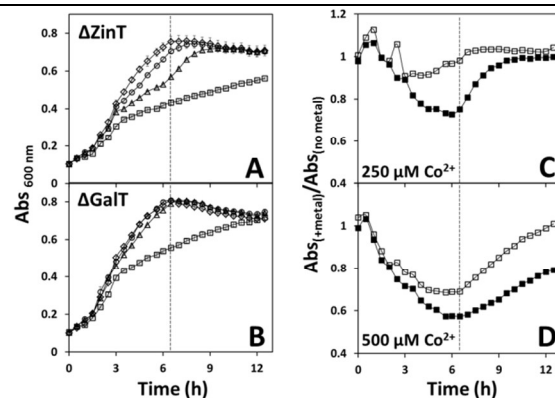

Figure 2. ZinT affords *E. coli* resistance to cobalt. Cells were grown aerobically in LB medium supplemented with 25 mg/L kanamycin at 37°C and the metal added at time 0. Panels A and B: growth curves of *E. coli* ΔzinT (Panel A) and ΔgalT (Panel B) strains in the presence of different concentrations of Co^{2+}: 0 μM (diamonds), 100 μM (circles), 250 μM (triangles) and 500 μM (squares). Panels C and D: normalized growth ratio Abs_{600nm}(+metal)/Abs_{600nm}(no metal) of ΔzinT (full squares) and ΔgalT (hollow squares) in the presence of 250 μM Co^{2+} (panel C) and 500 μM Co^{2+} (panel D). Dashed lines depict the start of the stationary growth phase. Data represent the mean±SD of four independent experiments.

These results show for the first time the involvement of ZinT in cobalt resistance. *E. coli* relies on the efflux systems RcnA and RcnB [28-30], two proteins transcriptionally regulated by the cobalt and nickel induced RcnR [28], to cope with high concentrations of cobalt. This system represents a defense against toxic reactivity of cobalt with Fe-S clusters from essential proteins and the oxidizing effect of this metal [7]. In light of our results, ZinT may have an important role in the response to excess Co^{2+}, which may be directly or indirectly transferred to RcnA/B to be excreted out of the cell.

Mercury was able to completely abrogate growth of both the ΔzinT and the control strains at 40 μM (data not shown), in line with its widely recognized toxicity [5, 31]. However, at 20 μM Hg^{2+}, a transient growth inhibition was observed for both strains, followed by a nearly full recovery of the control strain in contrast with the lower growth rate of the ΔzinT strain (Figures 3A, B and D). No significant differences between strains were observed at 15 μM Hg^{2+} (Figure 3C). Mercury resistance in bacteria involves a group of proteins from the Mer family, responsible for the transport of Hg^{2+} (MerC, MerE, MerF, MerP, MerT) and its reduction to Hg^0 by mercuric reductase (MerA) [32, 33]. Volatile Hg^0 is non-toxic and freely diffuses out of the cell. ZinT now appears as an auxiliary component of this complex resistance mechanism, using its high affinity towards mercury to trap Hg^{2+} ions before metabolization.
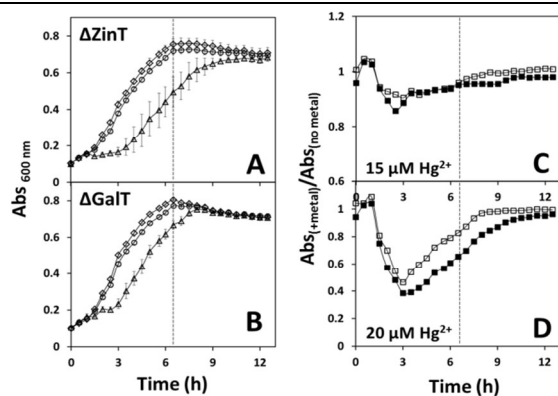
Figure 3. Resistance of mutant *E. coli* strains to mercury. Cells were grown aerobically in LB medium supplemented with 25 mg/L kanamycin at 37°C and the metal added at time 0. Panels A and B: growth curves of Δ*zinT* (Panel A) and Δ*galT* (Panel B) in the presence of different concentrations of Hg^{2+}: 0 μM (diamonds), 15 μM (circles) and 20 μM (triangles). Panels C and D: normalized growth ratio Abs_{600nm}(+metal)/Abs_{600nm}(no metal) of Δ*zinT* (full squares) and Δ*galT* (hollow squares) in the presence of 15 μM Hg^{2+} (panel C) and 20 μM Hg^{2+} (panel D). Dashed lines depict the start of the stationary growth phase. Data represent the mean±SD of four independent experiments.
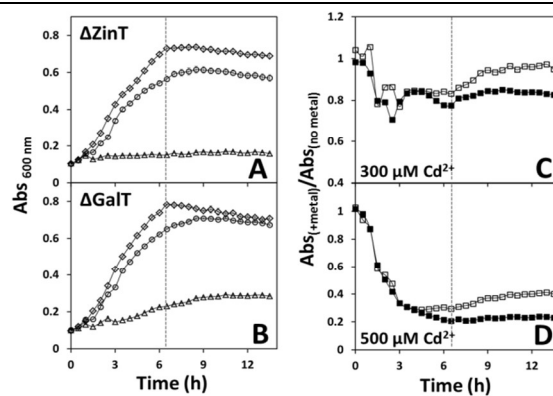

Figure 4. Resistance of mutant *E. coli* strains to cadmium. Cells were grown aerobically in LB medium supplemented with 25 mg/L kanamycin at 37°C and the metal added at time 0. Panels A and B: growth curves of Δ*zinT* (Panel A) and Δ*galT* (Panel B) in the presence of different concentrations of Cd^{2+}: 0 μM (diamonds), 300 μM (circles) and 500 μM (triangles). Panels C and D: normalized growth ratio Abs_{600nm}(+metal)/Abs_{600nm}(no metal) of Δ*zinT* (full squares) and Δ*galT* (hollow squares) in the presence of 300 μM Cd^{2+} (panel C) and 500 μM Cd^{2+} (panel D). Dashed lines depict the start of the stationary growth phase. Data represent the mean±SD of four independent experiments.

ZinT was first described as a cadmium-binding protein, transcriptionally induced by cadmium stress [14]. However, more recent studies have shown contradictory data regarding the role of this protein as a defense mechanism protecting the cell from cadmium poisoning [20, 21]. Our results clearly show that *E. coli* relies on ZinT to cope with moderate cadmium concentrations (Figure 4). At 300 μM Cd^{2+} the growth of both strains is delayed, the Δ*galT* control showing a more efficient recovery within seven hours of cadmium challenge (Figures 4A, B and C). At a higher concentration of this metal (500 μM), however, the growth of the *zinT*-null strain is completely blocked, whereas the control strain is capable of keeping a slow, yet constant growth rate (Figures 4A, B and D). Cadmium is an extremely toxic element, not only due to its mutagenic effect [8] but also to its ability to generate ROS. Although it is not a redox active compound prone to undergo Fenton reactions, its reactivity towards protein Fe-S clusters causes Fe^{2+} to be released, triggering oxidative stress [5]. Attempting to counteract these effects, *E. coli* uses the Zn-translocating P-type ATPase ZntA to export cadmium [34, 35], implying that mechanisms of zinc and cadmium resistance are closely related.

The presence of 3 mM copper in the culture medium was found to nearly arrest the growth of Δ*zinT* while allowing a slow recovery of the control strain (Supplementary Figure S2). However, no differences between strains were observed at lower Cu^{2+} concentrations whereas higher concentrations (5 mM) proved to be lethal for both strains (data not shown). These data are in line with a previous study by Kershaw et al. [20] showing an altered expression of the *zinT* gene in the presence of high concentrations of copper and a deficient growth of a *zinT*-deleted strain. However, the high concentration of Cu^{2+} required in order to observe a difference between strains and the lethal effect of low millimolar copper concentrations in *E. coli* cultured in LB [36] make these observations hardly compatible with a putative physiological role of ZinT in copper metabolism.

In contrast with the proven ability of ZinT to bind nickel, no effect was found on the growth rate of the Δ*zinT* mutant as compared to the control strain (Supplementary Figure S3).

The presence of a natural N-terminal histidine tag together with the inner histidine side chains may explain the protein's high affinity towards Ni^{2+} ions, although no biological effect on nickel poisoning or starvation has been established.

The role of ZinT in zinc metabolism is yet far from being completely understood. While its importance is established in zinc deficient conditions, recruiting zinc from the periplasm to be transferred for the import system ZnuABC or other proteins requiring this metal [18, 19, 24, 25], no evidence was found for a detoxification mechanism at higher zinc concentrations [21]. Our results show only a slight advantage of the Δ*zinT* strain during the exponential phase at 600 μM Zn^{2+} (Supplementary Figure S4). This nearly indistinguishable behavior between strains allows us to support the idea that zinc efflux systems, namely ZntA, are able to cope with toxic concentrations of zinc independently of ZinT [20, 34, 37].

Structural insights into metal binding by ZinT

The *Escherichia coli* ZinT crystal structure was solved bound to Zn^{2+} at 1.79 Å resolution (PDB code: 5AQ6). ZinT crystals belong to the tetragonal space group ($P4_12_12$) with one molecule in the asymmetric unit. The ZinT overall structure closely resembles previously reported models [16] (e.g., superposition, using CCP4 suite [38], with 1OEK: Quality Q: 0.90 with an r.m.s.d. of 0.64 Å for 182 aligned Cα atoms; and 1S7D Quality Q: 0.96, with an r.m.s.d. of 0.47 Å for 187 aligned Cα atoms). Each monomer consists of two domains: *i)* the calyx domain, an antiparallel up-down β-barrel comprising eight β-strands ($β_A$ to $β_H$) flanked by one α-helix with overall dimensions of 45 Å × 39 Å × 31 Å, and, *ii)* a smaller wide open helical domain at the side of the calyx β-barrel – the helix domain, with a deep cleft running down through it. The final ZinT model comprises 190 residues (Ser5–His193, mature protein numbering employed henceforth, and His1 - detailed below) with clear electronic density for all residues, except the N-terminally located Gly2-His3-His4 residues, as in previously deposited structures. The N-terminus is thought to be very mobile in these proteins, which is why the thus far deposited models miss this region [16, 17]. The model also contains 181
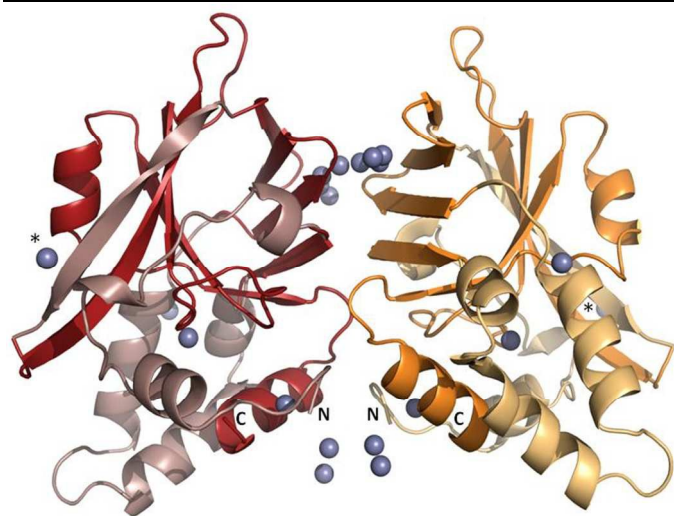
Figure 5. ZinT crystallographic dimer. Ribbon diagram of ZinT crystallographic dimer [PDB code: 5AQ6] showing all zinc atoms (represented as blue spheres) bound by and between each monomer within the dimer. The two structural regions are shown in different colour tones: the calyx domain (dark tone) and the open helical domain (light tone). In the centre top part, a chain comprising six zinc ions (three per monomer, where one zinc is in two different conformations) located between the beta alleyway within each monomer, making up a total of eight zinc ions in the dimer. In the bottom center part, four zinc ions (two per monomer) are loosely bound at the ZinT N-termini. Each monomer also binds two zincs in the canonical cluster, one near the C–terminus, and another one buried deep inside the ZinT cleft. Finally, an extra zinc is coordinated between a different crystallographic dimer (the symmetric zinc is also represented as *).

water molecules, one acetate and 8 zinc ions bound either to histidines or carboxylate residues. Full zinc metal content in ZinT was confirmed by X-ray fluorescence (XRF) measurements on protein solution and ZinT crystals, which through the online collection and qualitative analysis of ZinT crystals XRF spectra revealed the occurrence of zinc in the crystal, with no traces of other metals either in the protein solution or the crystals. The model has been refined to R_{work} 17.4 % and R_{free} 20.8 %.

Since ZinT was isolated as a dimer, the plausibility of the symmetry-generated dimer (Figure 5) was further confirmed by employing CCP4 jsPISA (surface area = 19680 Å^2; buried area = 3140 Å^2; $\Delta G_{interaction}$ = -410 Kcal/mol; $\Delta G_{dissociation}$ = 30.1 Kcal/mol).

The 'canonical' cluster harbors two zincs
The location of all metal binding sites was confirmed by solving the structure by the SAD method using the anomalous signal from data collected at 1 Å. In all available ZinT structures, a canonical metal cluster located in the calyx domain topped by the helical domain may harbor up to two metal ions. In the structure herein reported, one zinc (Zn_1) is coordinated by His144, His153 and His155 (Figure 6A), the same ligands as described for *S. enterica* zinc-bound ZinT (PDB 4AYH) [17] and *E. coli* structures co-crystallized with cadmium, nickel and zinc (PDB 1OEE, 1OEJ and 1TXL respectively) [16]. Although the metal coordination appears to be completed by neighboring water molecules, the geometry cannot be clearly defined due to local disorder. A second zinc ion (Zn_2) is herein found coordinated by His6, His193, Glu189 and one extra histidine (Figure 6). In the N-terminal region, the electron density for the
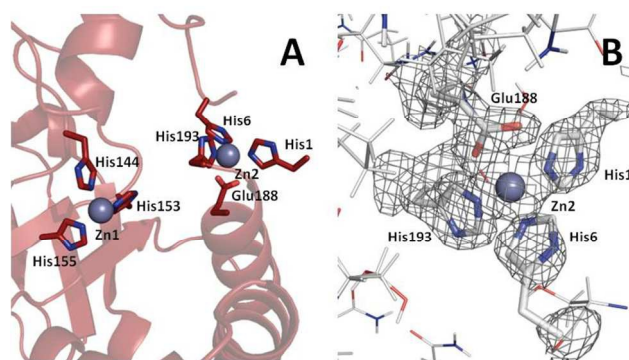

Figure 6. Zinc coordinated to the ZinT canonical site. Zinc ions bound in the canonical cluster. Panel A: ZinT monomer with two zinc atoms bound in the canonical cluster in a tetragonal conformation. The most buried zinc is coordinated by His144, His153, His155 and disordered water molecules (waters not shown). The second zinc is coordinated by His6, His193, Glu188 and loose His1 residue. Panel B: Electronic density around the second binding site (in the canonical cluster) showing clear density for His1.

protein backbone is poorly defined for the first 5 residues. However, an imidazole-shaped electron density feature is clearly observed completing the tetrahedral coordination of this second metal center, proposed to belong to His1 (Figure 6B). Despite common features of this canonical cluster, a degree of variability in terms of coordination can be observed. In two *E. coli* ZinT structures (PDBs 1OEK and 1S7D), Zn_A is coordinated by His144, His155 and disordered waters, whereas Zn_B is coordinated by His153, His193, Glu189 and nearby water(s) [16]. Furthermore, in the structure of a Ni-bound *E. coli* ZinT (4TNN), to date the only one with a completely ordered histidine-rich N-terminal section, nickel coordination is ensured by His144, His153 and His193, and His1 and His4 from the N-terminus of a symmetry-related molecule. While the reasons for the variable zinc coordination spheres in the different structures remain elusive, this variability reinforces the notion that this region is capable of adopting different conformations, with possible impact in metal affinity and selectivity.

The unstructured N-terminal binds extra zinc ions
An extra anomalous signal observed at the N-terminal region of the ZinT structure here described clearly shows the presence of two more zinc ions per monomer, surrounded by a strong electron density, which could not be clearly assigned. This is an indication that despite being a highly flexible region, this histidine-rich N-terminal is able to accommodate extra metal ions besides the two zinc sites in the canonical cluster. Considering the crystallographic dimer, two symmetry-related N-terminal regions are brought together coordinating these four extra zinc ions (two per monomer). While in the structure herein reported only one of the zinc ions from each pair has a clearly identified ligand (Glu188), the weak electron density for the protein chain in this region allowed the generation of an unrefined structural model which places His3 as a possible ligand for the same zinc, whereas the nearby zinc ion may be coordinated by His4. Due to the close proximity of both N-termini, extra interactions between the symmetry-related molecules could be involved in stabilizing zinc ions in this region. Since this weak electron density precludes a precise identification of the side chains most likely coordinating the extra zinc ions, this interpretation of the weak electron density leaves room for other conformations.
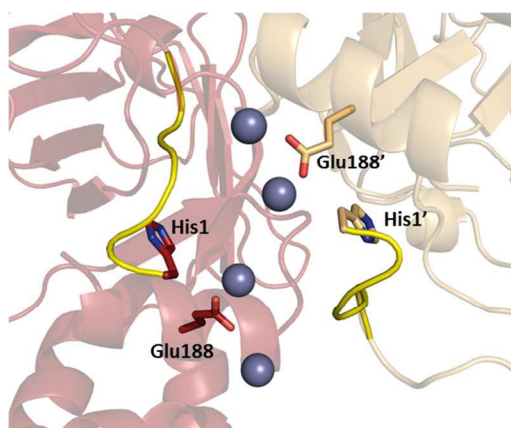
Figure 7. Unstructured N-terminus. Bottom view of ZinT dimer showing the highly flexible region of the N-termini of both monomers close to each other, coordinating two extra zinc ions. One of the zinc ions is coordinated by Glu188 and the other is most likely coordinated by histidines (His3 or 4) present in the His-rich N-terminus. Yellow tubes represent unmodelled region showing a putative main chain in a possible conformation based on weak electron density, yet insufficient to model the side chains

This N-terminal zinc cluster has never been observed in previously reported ZinT structures. Since these zinc ions are located in a highly flexible region, the structure herein reported could represent the crystallographic trapping of a physiological intermediate where the histidine-rich N-terminus forages zinc ions from the medium *en route* to the canonical cluster for storage [18].

Other interactions also appear plausible, as judged from other available crystal structures. In the structure of *E. coli* ZinT co-crystallized with Ni (PDB 4TNN), the His-rich stretch of one molecule enters the cleft of a symmetry-related molecule and enriches Ni coordination at its canonical site. A related proposal was based on a SAXS model of *S. enterica* ZinT in complex with ZnuA, a soluble domain of the ZnuABC transporter complex, where the ZinT cavity near the canonical cluster is occupied by the histidine-rich loop of ZnuA [17, 24]. The interaction between ZnuA and ZinT is related to the putative zinc transport from ZinT to the ZnuABC transporter. Other studies further highlight the strong interaction between ZinT and ZnuA in the zinc uptake pathway [18].

The 'outsider' zinc binding site

The ZinT structure herein described contains a third zinc site (marked with an asterisk in Figure 5) previously identified solely in one zinc-containing *E. coli* ZinT structure (1OEK) [16]. This site is located at the protein surface and mediates contacts between helix domains of symmetry-related molecules different from the physiological dimer herein proposed. In the structure reported here, this zinc ion is coordinated by His75 in one molecule and by Asp24 in its symmetry-related mate. An acetate molecule likely derived from the crystallization buffer acts as the third coordinating ligand, whereas in 1OEK this coordination position is assumed by the carbamoyl oxygen from Gln47. The fact that this zinc site coordination is shared between non-physiological symmetry mates and that an acetate ion can assume the third coordination position suggests this site to be a crystallization artifact unlikely to have a physiological role.

The zinc 'chain gang'

A unique feature in the structure here reported is a chain of zinc ions located at the solvent-exposed flank of the β-barrel from the calyx domain, opposite the N-terminal, at the dimer interface referred to henceforth as the beta alleyway (Fig 8). Each monomer harbors three zinc ions, one of which is found in two alternate positions, like its ligands Glu88 and His95. Considering the dimer, an ion chain with eight zincs is obtained, whose physiological role remains to be elucidated. The fact that within each monomer one of these zinc ions is present in two alternate positions, together with the partial occupation displayed by all Zn sites, suggests a certain degree of positional mobility within this chain. The central zinc in the chain (sym_Zn5, i.e., Zn5 from a symmetry-related monomer) is likely coordinated by conformers A of Glu88 and sym_Glu93 (Fig. 8). The second zinc (Zn3) has two conformations: Zn3A coordinated by His95 (conformer A) and sym_Asp89; and Zn3B coordinated by Glu93 and B conformers of His95 and sym_Glu88B. Finally, the third zinc (sym_Zn8) is coordinated by Asp89 (Fig 8). This protein region was previously observed to coordinate metal ions, but limited to one or two sites.

The zinc-loaded structure (PDB 1OEK) crystallized in the $P4_12_12$ space group and therefore displayed the same crystallographic dimer as the ZinT structure described here. However, whereas in the present structure the anomalous signal clearly indicates the presence of three zinc ions in each molecule, in PDB 1OEK only one zinc is coordinated by His95 and the physiological symmetry mate residue sym_Glu93. Notably, the higher zinc load of the present structure in comparison with 1OEK is unlikely to derive from the zinc concentrations in the crystallization conditions: ~38 mM in this work and 100 mM Zn^{2+} in 1OEK.
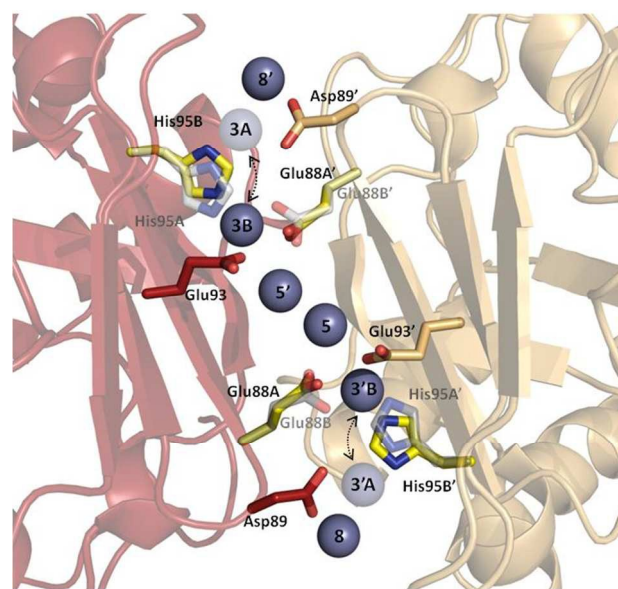
Figure 8. Zinc chain located on top of the dimer interface. Beta alleyway top view of the putative zinc channel. A ZinT dimer coordinates 6 zincs with carboxylate residues and His95 although all 8 zinc observed positions are represented here. His95A (transparent) and Glu88B (full) are respectively coordinating Zn3A and Zn5. His95B (full), Glu93 (full) and Glu88A' (transparent) coordinate Zn3B, while Asp89 coordinates the distal Zn8. Histidines A and B conformers were discriminated by pointing the nitrogen atom towards the metal maintaining the imidazole ring parallel to the bond direction.

As for the Cd-loaded ZinT structure (PDB 1OEE), it was reported to have a completely flipped dimer arrangement with respect to the structure now presented. This flipped dimer accommodates two cadmium ions in the same region of the zinc 'chain', although one side of the beta 'alleyway' is replaced by helix α6 containing Glu185 and Glu188, which in the present ZinT structure are ligands of the 'unstructured' N-terminal zinc cluster.

Although at this stage we cannot completely exclude the possibility of a crystallization artifact, different lines of evidence point to previously unraveled real zinc-binding sites. The putative physiological dimer assembles in solution with ZinT purified in the absence of zinc. Therefore, it appears more likely that dimerization enables the extra binding sites with ligands from both monomers, rather than the extra zinc forcing dimerization. Moreover, these extra zinc sites are observed with almost 3-fold lower zinc concentration as compared to crystallization conditions yielding a single zinc site in this region. In summary, the extra zinc sites available only upon assembly of the physiological dimer may here be stabilized by subtle changes in protein preparation or the different crystallization pH, despite possibly reflecting a trapped intermediate physiological state.

Experimental

Production and purification of *E. coli* ZinT

Escherichia coli ZinT was isolated while attempting to produce recombinant *Entamoeba histolytica* EHI_16450, as discussed above. The EHI_165450 gene [39] was PCR amplified from *Entamoeba histolytica* HM-1:IMSS genomic DNA using the forward primer 5'- CCTAGGATGAGTGACATCAACAACAACATT and the reverse primer 5'- GGATCCTTAATCAATTTCTATTTTATTCACCTT, both containing the AvrII restriction site (underlined). The PCR product was cloned into the Topo TA pCR2.1 vector (Invitrogen) and digested with the NheI restriction enzyme (New England Biolabs). After gel purification the DNA fragment was sub cloned into the pET28a expression vector (Clontech Laboratories) at the NheI restriction site yielding an N-terminally 6xHis-tagged construct. The resulting vector was used to transform *Escherichia coli* BL21 (DE3) Rosetta cells. Cells were grown at 37°C in M9 minimal medium containing 25 mg/L kanamycin (Nzytech) and 34 mg/L chloramphenicol (Nzytech) until the OD_{600nm} reached 0.3. Protein expression was induced by addition of 0.1 mM isopropyl-β-D-thiogalactoside (Nzytech) followed by 4h-incubation at 30°C. Cells were then harvested and the pellet resuspended in buffer A (50 mM KPi, 300 mM KCl, pH 7.5, 10% glycerol, 10 mL/L culture) containing 1 mg/mL lysozyme (AppliChem), 1 mM phenylmethylsulfonyl fluoride (Merck) and deoxyribonuclease I (AppliChem). After incubation on ice for 30 min, cells were disrupted by sonication, centrifuged at 8,200 ×g (5 min, 4°C) and imidazole was added to the supernatant to a final concentration of 10 mM. All purification steps were carried out on an Äkta Prime FPLC system (GE Healthcare). Affinity purification of the 'naturally tagged' protein was performed using a HisTrap FF crude 1-mL column (GE Healthcare) previously equilibrated with buffer A containing 10 mM imidazole (buffer B). The cleared supernatant was loaded into the column at 1 mL/min and the column was washed with 25 column volumes of buffer B followed by a linear imidazole gradient of 15 column volumes to a final concentration of 500 mM. Pooled protein fractions were loaded into a PD10

desalting column (GE Healthcare) for imidazole removal and concentrated using a Vivaspin 15R 10 kDa tube (Sartorius). The protein was further purified by gel filtration using a HiLoad 26/600 Superdex S200 column (GE Healthcare) previously equilibrated with buffer A. The obtained protein was analyzed by SDS-PAGE and its concentration determined by the Bradford method [40]. The identity of ZinT was only revealed upon obtaining its crystallographic structure, as detailed below.

Differential scanning fluorimetry

The effect of heavy metals on the protein's thermal denaturation profile was assessed by DSF. Assays were carried out in 96-well white opaque plates, each well containing 0.2 µg/µL of purified ZinT in 100 mM HEPES, pH 7.0, 10 to 500 µM of the metal (Supplementary Table 1) to be analyzed and a 1:1000 dilution of the fluorescent probe SYPRO orange (commercially available from Invitrogen at a 5000x working concentration). Final buffer composition in the mixture: 12.5 mM KPi, 75 mM KCl, 2.5% glycerol, 75 mM HEPES. The mixture was incubated at 20°C for 10 minutes followed by a temperature gradient of 1°C/minute or 0.1°C/second from 20°C to 95°C using either a CFX96 or an iQ5 Real Time PCR detection system (Biorad) and the fluorescence emission was detected using the HEX channel (λ_{exc} 515-535 nm and λ_{em} 560-580 nm). In order to determine the melting temperature (T_m), the obtained thermal unfolding curves were analysed using Prism 6 (GraphPad Software, Inc.) with either a monophasic or biphasic sigmoidal fit.

Metal sensitivity of bacterial strains

Stock solutions of $NiSO_4.6H_2O$ (Applichem), $HgCl_2$, $CuCl_2.2H_2O$, $CoCl_2.6H_2O$, $ZnSO_4.7H_2O$ and $CdCl_2.21/2H_2O$ (all from Merck) were prepared in ultrapure sterile H_2O and diluted in Luria-Bertani medium with 25 mg/L kanamycin (LB+kan). The Escherichia coli JW1956-1 strain [41] carrying a deletion for the *zinT* gene (Δ*zinT*) was purchased from the *E. coli* Genetic Stock Center (Yale University, CT, USA). The JW0741-1 strain carrying a deletion for the *galT* gene (Δ*galT*) was used as a control. To determine the growth rate in the presence of metals, both strains were grown at 37°C in in LB+kan until an Abs_{600nm} ~ 0.2 was reached, when 50 µL of culture were transferred into a 96-well plate and 50 µL of the appropriate concentration of metal were added. Each condition was replicated in four wells. The plate was incubated at 37°C at 600 rpm in a Titramax 100 vibrating platform shaker (Heidolph) and the Abs600nm recorded every 30 minutes using a microplate reader (Asys Expert Plus).

Crystallization and structure determination

ZinT crystals were obtained at 302K by the sitting-drop vapour diffusion method, mixing 0.5 µl of a 9 mg/ml protein sample with an equal amount of reservoir solution containing 75 mM zinc acetate, 18 % PEG 3350. Crystals appeared within 7 days and grew for two weeks. Diffraction data from a flash-cooled crystal of *E. coli* ZinT (at the time believed to be of *Entamoeba histolytica* 879.m), cryo-preserved with 25% glycerol, were collected to 1.79 Å resolution at beamline ID29 of the European Synchrotron Radiation Facility (ESRF) in Grenoble using 1 Å wavelength X-rays and a PILATUS 6M detector. The crystal belonged to either the tetragonal space group $P4_12_12$ or its enantiomorph $P4_32_12$ with unit cell parameters a = 62.01 Å, c = 149.72 Å and two estimated *E. histolytica* 879.m monomers in the asymmetric unit. The data were integrated and scaled with XDS [42]. The diffracted intensities obtained with XDS were

subsequently merged with AIMLESS and converted to structure factors with CTRUNCATE in the CCP4 suite [38]. A random 5% sample of the reflection data was flagged for cross-validation using R-free [43]. The data collection and processing statistics are presented in Supplementary Tables 3 and 4. The data contain a significant anomalous signal, assumed to arise from the Zn^{2+} ions co-crystallized with the protein and therefore the structure was determined by the Single Wavelength Anomalous Dispersion (SAD) method. Using the HKL2MAP [44] graphical user interface, the SAD dataset was scaled and analysed with SHELXC, the Zn^{2+} sub-structure was determined with SHELXD using data to 2.5 Å resolution and the phase problem solved with SHELXE [45]. Although the best SHELXD solution gave correlation coefficients of only *ca.* 21%, the SHELXE calculations gave a clear discrimination between the correct and the inverted substructures. However, the resulting experimental electron density map lacked sufficient quality for automatic interpretation.

The phases derived from the SAD data were improved using the maximum-likelihood heavy-atom parameter refinement in autoSHARP [46]. A subsequent optimizing density modification procedure using SOLOMON [47] suggested only one *E. histolytica* 879.m monomer in the asymmetric unit of the crystal structure and a solvent content of 56.1%. A partial unrefined model containing 195 residues in 3 chains, of which 138 were sequenced, was automatically built with BUCCANEER [48] within autoSHARP. Despite the high values of R and R free (50.3 % and 53.9 % respectively) the fact that one continuous chain with 125 aminoacid residues was obtained was taken as an indication that the model could be corrected manually. However, inspection of the model and the density-modified electron-density maps with COOT [49] clearly indicated that the structure determined was not of *Entamoeba histolytica* 879.m. A continuous polypeptide chain containing 188 aminoacids was manually built in COOT and tentatively sequenced based on the density-modified electron density map. The sequence was input to the NCBI BLAST server (http://www.ebi.ac.uk/Tools/sss/ncbiblast) at the European Bioinformatics Institute (EBI) and the result was a near perfect match with *E. coli* ZinT. Prior to the refinement, the model was corrected according to the *E. coli* ZinT sequence.

The crystal structure of *E. coli* ZinT was refined at 1.79 Å using PHENIX v.1.8.4 [50]. Throughout the refinement, the model was periodically checked and corrected with COOT against the 2|Fo|-|Fc| and |Fo|-|Fc| electron-density maps. After the first refinement with hydrogens and optimized weights in PHENIX, BUSTER [51] was employed to improve the electron density map particularly of the N-terminal region, and manual building using COOT [49] against the |Fo|-|Fc| electron density map was only possible from Ser5 onwards. Although the electron density map in the region of residues 2-4 was not good enough for manual building, His1 was included in the model because of a clear and well defined electron density map for its side-chain imidazole moiety. A total of 220 solvent molecules were included in the refinement, located by the PHENIX AUTOBUILD procedure and by inspection of the |Fo|-|Fc| electron-density maps. PHENIX READYSET tool was used to impose restrains in the ligations of residues binding zinc atoms. In the final refinement cycles, the model was refined using translation-libration-screws (TLS, [52]) rigid body refinement of anisotropic displacement parameters (ADP). Automated analysis of the refined isotropic ADPs by PHENIX led to the subdivision of the protein into six TLS rigid bodies. The final values of R and R-free [43] were 0.173 and 0.203 respectively.

The maximum likelihood estimate of the overall coordinate error was 0.18 Å. The refinement statistics are presented in Supplementary Table 4. The structure was analysed with MOLPROBITY [53] and there were no outliers in a Ramachandran [54] j,f plot. The coordinates and structure factors have been submitted to the Protein Data Bank [55] with accession code 5AQ6.

Conclusions

The work herein described reports the implementation of an experimental platform to structurally and functionally evaluate metal binding to the *Escherichia coli* ZinT, a protein involved in zinc homeostasis, with putative roles in the detoxification of other metals, as confirmed by our studies.

Screening of different metals potentially binding to isolated ZinT was carried out employing a fast, straightforward and medium-throughput fluorescence-based thermal shift assay. The acquired data are in full accordance with previous studies analysing ZinT metal affinity by other methods, such as mass spectrometry or size-exclusion chromatography, and allowed selecting a set of metal ions to be further studied in terms of ZinT function in metal toxicity alleviation. To this end, we analysed in 96-well plates the sensitivity of two mutant *E. coli* strains deleted either in *zinT* or in the unrelated gene *galT*, to different concentrations of the selected metals. The resulting growth curves allowed proposing previously undisclosed roles of ZinT in cobalt, mercury and cadmium resistance. The joint results from the protein- and cell-based assays suggest that in addition to the role of ZinT in zinc homeostasis, whenever cobalt, cadmium or mercury are present at sub-lethal toxic concentrations, ZinT will serve as a supplementary metal storage that will feed the appropriate efflux proteins, thus protecting the cell from toxic events.

Complementing the functional studies, the crystallographic structure of zinc-loaded ZinT solved at 1.79 Å resolution is herein reported, presenting unique features in terms of the zinc binding sites, despite the overall similarities with previously described models. Indeed, a number of bound zinc ions have been found that were not previously observed in other crystallographic structures. Metal analysis of recombinant ZinT fused to maltose-binding protein (MBP) yielded ~4 zinc ions per monomer, upon incubation with 10 molar equivalent of Zn^{2+} [56], somewhat consistently with previous crystallographic data. However, the large MBP tag may impair zinc loading into the novel clusters herein observed, obtained with the native non-recombinant protein. The unequivocal assignment of these zinc ions, both at the unstructured N-terminal cluster and in the 'chain' cluster, characterized by partial occupancies and with a high degree of mobility, is fully consistent with the hypothesis of metal ions being only temporarily stabilized before storage, transfer to other proteins, or metal efflux to prevent toxicity. The combined structural and functional information herein described shed new light into the ZinT metal binding mechanism and show its multi-faceted role in metal toxicity alleviation.

Acknowledgements

Metallomics Accepted Manuscript

Supplementary Figure S1. Sequence alignment of *Escherichia coli* ZinT and homologues from different bacterial species. The red box highlights the conserved histidine-rich domain.

Supplementary Figure S2. Resistance of mutant *E. coli* strains to copper. Cells were grown aerobically in LB medium supplemented with 25 mg/L kanamycin at 37°C and the metal added at time 0. Panel A: growth curve of $\Delta zinT$ in the absence (diamonds) or presence (circles) of 3 mM Cu^{2+}. Panel B: growth curve of $\Delta galT$ in the absence (diamonds) or presence (circles) of 3 mM Cu^{2+}. Panel C: normalized growth ratio Abs_{600nm}(+metal)/Abs_{600nm}(no metal) of $\Delta zinT$ (full squares) and $\Delta galT$ (hollow squares) in the presence of 3 mM Cu^{2+}. Dashed lines depict the start of the stationary growth phase. Data represent the mean±SD of four independent experiments.

Supplementary Figure S3. Resistance of mutant *E. coli* strains to nickel. Cells were grown aerobically in LB medium supplemented with 25 mg/L kanamycin at 37°C and the metal added at time 0. Panel A: growth curve of $\Delta zinT$ in the absence (diamonds) or presence (circles) of 1 mM Ni^{2+}. Panel B: growth curve of $\Delta galT$ in the absence (diamonds) or presence (circles) of 1 mM Ni^{2+}. Panel C: normalized growth ratio Abs_{600nm}(+metal)/Abs_{600nm}(no metal) of $\Delta zinT$ (full squares) and $\Delta galT$ (hollow squares) in the presence of 1 mM Ni^{2+}. Dashed lines depict the start of the stationary growth phase. Data represent the mean±SD of four independent experiments.

Supplementary Figure S4. Resistance of mutant *E. coli* strains to zinc. Cells were grown aerobically in LB medium supplemented with 25 mg/L kanamycin at 37°C and the metal added at time 0. Panels A and B: growth curves of $\Delta zinT$ (Panel A) and $\Delta galT$ (Panel B) in the presence of different concentrations of Zn^{2+}: 0 μM (diamonds), 600 μM (circles) and 800 μM (triangles). Panels C and D: normalized growth ratio Abs_{600nm}(+metal)/Abs_{600nm}(no metal) of $\Delta zinT$ (full squares) and $\Delta galT$ (hollow squares) in the presence of 600 μM Zn^{2+} (panel C) and 800 μM Zn^{2+} (panel D). Dashed lines depict the start of the stationary growth phase. Data represent the mean±SD of four independent experiments.

Notes and references

[a] Research Institute for Medicines (iMed.ULisboa), Faculty of Pharmacy, University of Lisbon, Portugal.

[b] Instituto de Biologia Experimental e Tecnológica, Apartado 12, 2781-901 Oeiras, Portugal.

[c] Instituto de Tecnologia Química e Biológica António Xavier, Universidade Nova de Lisboa, Av. da República, 2780-157 Oeiras , Portugal.

Electronic Supplementary Information (ESI) available:

Supplementary Table 1 - Effect of metals on ZinT thermal denaturation profiles tested by differential scanning fluorimetry.

Supplementary Table 2 - Metal concentrations supplemented into growth medium of $\Delta zinT$ and $\Delta galT$ *Escherichia coli* strains.

Supplementary Table 3 - Crystallographic data collection and processing statistics.

Supplementary Table 4 - Final refinement statistics.

Supplementary Figure S1 - Protein sequence alignment.

Supplementary Figure S2 - Resistance of mutant *E. coli* strains to copper.

Supplementary Figure S3. Resistance of mutant *E. coli* strains to nickel.

Supplementary Figure S4. Resistance of mutant *E. coli* strains to zinc.

References

1. G. Grass, C. Rensing and M. Solioz, *Applied and environmental microbiology*, 2011, **77**, 1541-1547.
2. C. Martin, W. L. Low, A. Gupta, M. C. Amin, I. Radecka, S. T. Britland, P. Raj and K. M. Kenward, *Current pharmaceutical design*, 2015, **21**, 43-66.
3. S. M. Quintal, Q. A. dePaula and N. P. Farrell, *Metallomics : integrated biometal science*, 2011, **3**, 121-139.
4. L. Macomber and J. A. Imlay, *Proceedings of the National Academy of Sciences of the United States of America*, 2009, **106**, 8344-8349.
5. F. F. Xu and J. A. Imlay, *Applied and environmental microbiology*, 2012, **78**, 3614-3621.
6. C. Ranquet, S. Ollagnier-de-Choudens, L. Loiseau, F. Barras and M. Fontecave, *The Journal of biological chemistry*, 2007, **282**, 30442-30451.
7. J. R. Fantino, B. Py, M. Fontecave and F. Barras, *Environmental microbiology*, 2010, **12**, 2846-2857.
8. Y. H. Jin, A. B. Clark, R. J. Slebos, H. Al-Refai, J. A. Taylor, T. A. Kunkel, M. A. Resnick and D. A. Gordenin, *Nature genetics*, 2003, **34**, 326-329.
9. L. Macomber and R. P. Hausinger, *Metallomics : integrated biometal science*, 2011, **3**, 1153-1162.
10. D. H. Nies, *FEMS microbiology reviews*, 2003, **27**, 313-339.
11. D. Osman and J. S. Cavet, *Natural product reports*, 2010, **27**, 668-680.
12. K. J. Waldron and N. J. Robinson, *Nature reviews. Microbiology*, 2009, **7**, 25-35.
13. P. Ferianc, A. Farewell and T. Nystrom, *Microbiology*, 1998, **144 (Pt 4)**, 1045-1050.
14. A. Puskarova, P. Ferianc, J. Kormanec, D. Homerova, A. Farewell and T. Nystrom, *Microbiology*, 2002, **148**, 3801-3811.
15. G. David, K. Blondeau, M. Renouard and A. Lewit-Bentley, *Acta crystallographica. Section D, Biological crystallography*, 2002, **58**, 1243-1245.
16. G. David, K. Blondeau, M. Schiltz, S. Penel and A. Lewit-Bentley, *The Journal of biological chemistry*, 2003, **278**, 43728-43735.
17. A. Ilari, F. Alaleona, G. Tria, P. Petrarca, A. Battistoni, C. Zamparelli, D. Verzili, M. Falconi and E. Chiancone, *Biochimica et biophysica acta*, 2014, **1840**, 535-544.
18. R. Gabbianelli, R. Scotti, S. Ammendola, P. Petrarca, L. Nicolini and A. Battistoni, *BMC microbiology*, 2011, **11**, 36.
19. A. I. Graham, S. Hunt, S. L. Stokes, N. Bramall, J. Bunch, A. G. Cox, C. W. McLeod and R. K. Poole, *The Journal of biological chemistry*, 2009, **284**, 18377-18389.

Metallomics Accepted Manuscript

20. C. J. Kershaw, N. L. Brown and J. L. Hobman, *Biochemical and biophysical research communications*, 2007, **364**, 66-71.

21. T. Stojnev, J. Harichova, P. Ferianc and T. Nystrom, *Current microbiology*, 2007, **55**, 99-104.

22. E. M. Panina, A. A. Mironov and M. S. Gelfand, *Proceedings of the National Academy of Sciences of the United States of America*, 2003, **100**, 9912-9917.

23. S. I. Patzer and K. Hantke, *The Journal of biological chemistry*, 2000, **275**, 24321-24332.

24. K. Hantke, *Current opinion in microbiology*, 2005, **8**, 196-202.

25. P. Petrarca, S. Ammendola, P. Pasquali and A. Battistoni, *Journal of bacteriology*, 2010, **192**, 1553-1564.

26. C. J. Kershaw, N. L. Brown, C. Constantinidou, M. D. Patel and J. L. Hobman, *Microbiology*, 2005, **151**, 1187-1198.

27. V. M. Bolanos-Garcia and O. R. Davies, *Biochimica et biophysica acta*, 2006, **1760**, 1304-1313.

28. D. Blaha, S. Arous, C. Bleriot, C. Dorel, M. A. Mandrand-Berthelot and A. Rodrigue, *Biochimie*, 2011, **93**, 434-439.

29. C. Bleriot, G. Effantin, F. Lagarde, M. A. Mandrand-Berthelot and A. Rodrigue, *Journal of bacteriology*, 2011, **193**, 3785-3793.

30. A. Rodrigue, G. Effantin and M. A. Mandrand-Berthelot, *Journal of bacteriology*, 2005, **187**, 2912-2916.

31. Y. Gao, X. Peng, J. Zhang, J. Zhao, Y. Li, Y. Li, B. Li, Y. Hu and Z. Chai, *Metallomics : integrated biometal science*, 2013, **5**, 913-919.

32. A. M. Nascimento and E. Chartone-Souza, *Genetics and molecular research : GMR*, 2003, **2**, 92-101.

33. Y. Sone, R. Nakamura, H. Pan-Hou, T. Itoh and M. Kiyono, *Biological & pharmaceutical bulletin*, 2013, **36**, 1835-1841.

34. C. Rensing, B. Mitra and B. P. Rosen, *Proceedings of the National Academy of Sciences of the United States of America*, 1997, **94**, 14326-14331.

35. R. Sharma, C. Rensing, B. P. Rosen and B. Mitra, *The Journal of biological chemistry*, 2000, **275**, 3873-3878.

36. G. Grass and C. Rensing, *Journal of bacteriology*, 2001, **183**, 2145-2147.

37. D. K. Blencowe and A. P. Morby, *FEMS microbiology reviews*, 2003, **27**, 291-311.

38. *Acta crystallographica. Section D, Biological crystallography*, 1994, **50**, 760-763.

39. J. B. Vicente, G. M. Ehrenkaufer, L. M. Saraiva, M. Teixeira and U. Singh, *Cellular microbiology*, 2009, **11**, 51-69.

40. M. M. Bradford, *Analytical biochemistry*, 1976, **72**, 248-254.

41. T. Baba, T. Ara, M. Hasegawa, Y. Takai, Y. Okumura, M. Baba, K. A. Datsenko, M. Tomita, B. L. Wanner and H. Mori, *Molecular systems biology*, 2006, **2**, 2006 0008.

42. W. Kabsch, *Acta crystallographica. Section D, Biological crystallography*, 2010, **66**, 125-132.

43. A. T. Brunger, *Nature*, 1992, **355**, 472-475.

44. T. Pape and T. R. Schneider, *J Appl Crystallogr*, 2004, **37**, 843-844.

45. G. M. Sheldrick, *Acta crystallographica. Section D, Biological crystallography*, 2010, **66**, 479-485.

46. C. Vonrhein, E. Blanc, P. Roversi and G. Bricogne, *Methods Mol Biol*, 2007, **364**, 215-230.

47. J. P. Abrahams and A. G. Leslie, *Acta crystallographica. Section D, Biological crystallography*, 1996, **52**, 30-42.

48. K. Cowtan, *Acta crystallographica. Section D, Biological crystallography*, 2006, **62**, 1002-1011.

49. P. Emsley and K. Cowtan, *Acta crystallographica. Section D, Biological crystallography*, 2004, **60**, 2126-2132.

50. P. D. Adams, P. V. Afonine, G. Bunkoczi, V. B. Chen, I. W. Davis, N. Echols, J. J. Headd, L. W. Hung, G. J. Kapral, R. W. Grosse-Kunstleve, A. J. McCoy, N. W. Moriarty, R. Oeffner, R. J. Read, D. C. Richardson, J. S. Richardson, T. C. Terwilliger and P. H. Zwart, *Acta crystallographica. Section D, Biological crystallography*, 2010, **66**, 213-221.

51. G. Bricogne, E. Blanc, M. Brandl, C. Flensburg, P. Keller, W. Paciorek, P. Roversi, A. Sharff, O. S. Smart, C. Vonrhein and T. O. Womack, 2011.

52. M. D. Winn, M. N. Isupov and G. N. Murshudov, *Acta crystallographica. Section D, Biological crystallography*, 2001, **57**, 122-133.

53. V. B. Chen, W. B. Arendall, 3rd, J. J. Headd, D. A. Keedy, R. M. Immormino, G. J. Kapral, L. W. Murray, J. S. Richardson and D. C. Richardson, *Acta crystallographica. Section D, Biological crystallography*, 2010, **66**, 12-21.

54. G. N. Ramachandran and V. Sasisekharan, *Adv Protein Chem*, 1968, **23**, 283-438.

55. H. M. Berman, J. Westbrook, Z. Feng, G. Gilliland, T. N. Bhat, H. Weissig, I. N. Shindyalov and P. E. Bourne, *Nucleic Acids Res*, 2000, **28**, 235-242.

56. M. P. Hensley, T. S. Gunasekera, J. A. Easton, T. K. Sigdel, S. A. Sugarbaker, L. Klingbeil, R. M. Breece, D. L. Tierney and M. W. Crowder, *J Inorg Biochem*, 2012, **111**, 164-172.